Journal of the European Ceramic Society 46 (2026) 118427

Contents lists available at ScienceDirect

Journal of the European Ceramic Society

journal homepage: www.elsevier.com/locate/jeurceramsoc

Assessing the feasibility of camphor-assisted Vat Photopolymerization of alumina for ultra-rapid debinding and sintering

Subhadip Bhandari [a,*], Alice Nicolini [a], Paolo Colombo [a], Vincenzo M. Sglavo [b], Mattia Biesuz [b], Giorgia Franchin [a]

[a] Department of Industrial Engineering, University of Padova, Via Marzolo 9, Padova 35131, Italy
[b] Department of Industrial Engineering, University of Trento, Via Sommarive 9, Trento 38122, Italy

ARTICLE INFO

Keywords:
Vat Photopolymerization
Stereolithography
Alumina
Camphor
Debinding
Ultra-Fast High Temperature Sintering

ABSTRACT

Vat Photopolymerization (VPP) enables the fabrication of complex ceramic components with a high resolution between 10 and 200 μm. However, the process is limited by slow thermal debinding and sintering. In this study, a new photosensitive alumina (Al_2O_3) resin was developed using camphor as a diluent to reduce viscosity, enabling successful printing at a high ceramic loading of 56 vol%. A comprehensive feedstock optimization strategy was implemented with a particular focus on rheological behaviour. Two geometries, a thin bowl (0.42 mm thick) and a cylinder (1.2 mm thick), were fabricated to investigate the influence of thickness on ultra-fast high-temperature sintering (UHS). Thin samples were debinded and sintered using a step-wise UHS profile, whereas thicker cylindrical parts required a separate debinding stage. Under optimized thermal conditions, both geometries achieved relative densities up to 97% without observable defects, demonstrating UHS as a rapid and energy-efficient alternative to conventional ceramic sintering.

1. Introduction

Traditional ceramic shaping technologies, such as slip casting, tape casting, injection molding, and die pressing, allow the fabrication of a green body that has to be sintered at high temperatures to achieve the desired densification and final properties [1,2]. These techniques present significant limitations in terms of design, long processing times and high costs [3]. Molds cannot produce structures with high geometrical complexity and tend to be extremely expensive, thus leading to high production costs.

These problems could be addressed with additive manufacturing (AM), also known as 3D printing. AM is defined by the ISO/ASTM standard 52900:2021(E) as the "process of joining materials to make parts from 3D model data, usually layer upon layer, as opposed to subtractive manufacturing and formative manufacturing methodologies" [4]. This revolutionary approach enables the fabrication of near-net-shape ceramic parts with complex geometries that are impossible to produce with traditional processing methods. Furthermore, the design of the manufactured components can be modified with ease without any physical intervention on the machine because no expensive tooling is required [2]. These characteristics make AM a particularly attractive alternative to traditional shaping technologies, especially for small production volumes such as prototyping [2].

Several ceramic AM technologies have been developed so far, including Vat Photopolymerization (VPP), Direct ink writing (DIW), Fused filament fabrication (FFF), Selective laser sintering (SLS), Binder jetting (BJ), among others [3,5]. Ceramic VPP stands out among the other families of ceramic AM technologies because it allows high resolution in the order of ~10 – 200 μm [6]. It is also one of the most established and commercialized processes in the AM market [6].

In general, a resin for ceramic VPP consists of the ceramic powder, monomer, photoinitiator (PI) and several other additives such as diluents and dispersant that may be added to improve the rheological properties of the suspension; these play an important role in determining the printability of the suspension [6,7]. Shear-thinning behavior, characterized by a decrease in viscosity when the shear rate increases, is common for suspensions with low-to-moderate solid loadings and ideal for VPP [7]. Conversely, a highly loaded ceramic suspension might exhibit shear-thickening behavior [7] and increased, uncontrolled light scattering [8].

A trade-off between the rheological properties and a high green density is therefore necessary to ensure a smooth printing process and

* Corresponding author.
E-mail address: subhadip.bhandari@phd.unipd.it (S. Bhandari).

https://doi.org/10.1016/j.jeurceramsoc.2026.118427
Received 10 January 2026; Received in revised form 13 April 2026; Accepted 14 April 2026
Available online 20 April 2026

desirable final sintered properties. Several studies have tried to overcome this trade-off by using diluents in the form of water [9], decalin [10], octanol [11], camphor [12,13], Gamma-Valerolactone [14], which decreases the viscosity of the ceramic resin and helps in achieving higher ceramic loadings in the photocurable resins, with additional benefits for further processing. In addition, the presence of a plasticizer can also facilitate the thermal debinding step by promoting pore formation at low temperatures and reduced heat release and gas evolution rates in inert atmosphere [15,16].

In FFF, typically one of the component in the thermoplastic blend can be partially dissolved in any organic solvent, leaving behind a small amount (8 – 10 wt%) of organics to be decomposed thermally [17,18]. On the contrary, in DIW, where water is used as a solvent for the paste preparation, it evaporates during drying, leaving behind only a small amount of organics (2 – 5 wt%) [19,20]. However, the monomers used in the VPP process cannot be removed by any means because of the thermosetting nature of the cured/crosslinked monomers. This leads to a comparatively higher binder content compared to DIW and FFF (after considering the solvent debinding). This makes the technology very sensitive to heating rates during the thermal debinding process.

Recently, Ultra-fast High-temperature Sintering (UHS) has been employed to debind and sinter additively manufactured components, enabling a drastic reduction of the processing time [17–22]. UHS is a pressureless consolidation technique where the sample is placed inside graphite felt that heats to high temperatures by Joule heating when the power supply is turned on [23]. The heat transfer from the felt to the sample occurs mostly by radiation, enabling ultra-rapid heating (around 10^3 – 10^4 °C/min) and cooling with enhanced densification within a few seconds [24–27].

This technique has been successfully demonstrated on components fabricated using FFF or DIW, resulting in defect-free and dense samples with optimized processing parameters [17–21]. Recently, there have been several studies dealing with UHS debinding and sintering of zirconia components fabricated with stereolithography [28,29]. The authors employed step-wise current ramps with intermediate holding times for the debinding and the sintering processes, enabling a gradual temperature increase and controlled release of the decomposed products. The sintered components exhibited similar density and mechanical/functional properties when compared to conventionally sintered components.

Moreover, these works have been carried out on commercially available resins (45 vol% [29] or 84.6 wt% [28]), where neither the components of the photocurable resin nor the initial ceramic powder characteristics are known, thereby limiting a detailed understanding of the feedstock design and processing conditions. In general, high-volume fraction of polymer in the green body increases the complexity of the debinding process, particularly in processes where significantly high heating rates are employed such as in UHS. Therefore, several studies have employed a prior thermal debinding step to ensure complete binder removal before subjecting the 3D-printed structures to UHS [30,31].

Herein, the present study is focused on the debinding and sintering studies of alumina components with camphor as a diluent fabricated using VPP process. The use of camphor enables to use a ceramic loading as high as 56 vol% (88.2 wt%) using a low-cost printer for polymeric materials. Such a high ceramic loading is highly beneficial for thermal post-processing. A thorough investigation of the different processing parameters and additives that can affect the rheology has been carried out. Printing parameters were optimized and then the printed samples were subjected to debinding and sintering via both conventional and UHS methods. It is to be noted that this study provides a proof-of-concept approach rather than constituting a systematic study on the UHS method limitations, since samples with different geometries were investigated and correspondingly different thermal treatment schedules were adopted.

Samples with thin walls were successfully debinded and sintered in multi-step UHS in 5 – 10 min, depending on the holding time at the final current, which is already significantly shorter or similar to the processing time reported in previous studies [28,29]. Nevertheless, thick wall samples exhibited defects with this multi-step approach. They were therefore debinded in a conventional furnace and then sintered using UHS, resulting in a finer microstructure and enhanced density when compared to their conventional counterparts. Such enhanced densification and finer microstructure were not achieved in the previous studies for samples processed using UHS [28,29].

2. Materials and methods

2.1. Materials

The ceramic powder used in this study consisted of commercial α-Al_2O_3 powder (CT 3000 LS SG, Almatis) with 99.8% purity, specific surface area equal to 7.80 m^2/g and median particle size (D_{50}) of 0.5 µm.

Several difunctional monomers were employed to optimize the resin formulation: 1,6-hexanediol diacrylate (HDDA), tetra(ethylene glycol) diacrylate (TEGDA), and two types of poly(ethylene glycol) diacrylate (PEGDA) with average molecular weights of 250 g/mol and 575 g/mol, respectively (PEGDA250 and PEGDA575). All chemicals were sourced from Sigma-Aldrich. Some of the most important properties relating to the monomers are reported in Table 1.

Bis (2,4,6-Trimethylbenzoyl) phenylphosphine oxide (Omnirad 819, IGM resins) was chosen as a photoinitiator. BYK-111 (BYK Chemie GmbH), a copolymer dispersant containing carboxyl and ester groups, was used to ensure homogeneous dispersion of the ceramic particles in the suspension, as reported in several other studies [33,34]. This phosphoric acid ester-based wetting and dispersing agent provides deflocculation through steric stabilization. Solid camphor ($C_{10}H_{16}O$, Regno Vegetale (Italy)) with a refractive index of 1.546 [35] was added to the formulation as a diluent.

Water, acetone, ethanol, isopropanol, 2-phenoxyethanol (TCI), and propylene carbonate (TCI) were evaluated as solvents to clean the samples after the printing process.

2.2. Choice of monomers and camphor solubility assessment

The optical transmittance of the different monomers was measured with a V-570 spectrophotometer (JASCO) to find the one with the optical properties more suitable for VPP.

Three resin formulations were prepared: HDDA/PEGDA250, HDDA/PEGDA575, and HDDA/TEGDA, all with a 1:1 monomer weight ratio. The solubility of camphor in each composition was estimated by preparing mixtures with different camphor contents. The considered resin/camphor ratios (in terms of weight) were 2, 1.7, 1.5 and 1.3

Table 1
Average properties of the monomers considered in this study. This data has been reported from Ref. [7,32] and the technical datasheet provided by the supplier.

Monomer	Molar mass [g/mol]	Density [g/mL] at 25 °C	Viscosity [mPa s]	Refractive index
HDDA	226	1.01	5 – 10	1.456
PEGDA 250	250	1.11	12	1.463
PEGDA 575	575	1.12	60	1.467
TEGDA	302	1.11	5 – 30	1.465

(corresponding to a camphor content of approximately 33 wt%, 37 wt%, 40 wt% and 43 wt% on the overall weight of the mixture). Camphor was dissolved in the resin with the help of a planetary mixer (ARE-250, THINKY) and its solubility was evaluated by visual analysis of the transparency of the mixture after 24 h.

The resin optimization process was carried out with the HDDA/PEGDA250 in 1:1 wt ratio because of better optical and rheological properties. A detailed explanation is provided in the results (Section 3.1, Section 3.2). The combination of HDDA and PEGDA250 also resulted in easier removal of the sample from the print head compared to the pure HDDA, and HDDA/TEGDA.

2.3. Preparation of the resin

Several resin formulations were prepared to study the effect of different constituents on the properties of the resin. In particular, the ceramic loading (48 – 58 vol%), the dispersant content (2 – 4 wt% of the ceramic powder), the monomer type, and the presence of camphor as a diluent were investigated. The photoinitiator concentration was always 1 wt% of the total monomer weight.

The liquid photocurable resin was prepared by first mixing the monomers and dispersant, then camphor was progressively added to the formulation. To ensure its complete dissolution, each addition was followed by mixing in the planetary mixer (ARE-250, THINKY) for 2 min at 2000 rpm. Once the mixture was homogenized, the alumina powder was gradually incorporated: a small amount of powder was poured into the resin and manually stirred, then the suspension was put into the planetary mixer at 2000 rpm for 2 min. These steps were repeated until all the ceramic particles were added and uniformly dispersed into the resin. A ball mill (Pulverisette 6 classic line, Fritsch) was then used to break down the agglomerates and further homogenize the resin. Several ball milling parameters, including the milling speed and duration, were varied to optimize the process. The speed of the ball milling was varied, but it could not exceed 350 rpm, otherwise, the resin would spill out of the jar. During this step, some of the ceramic resin was lost as it adheres to the milling balls and the ball milling container.

After ball milling, the ceramic resin was transferred to a container and the photoinitiator was added to the resin, which was then homogenized in the planetary mixer at 2000 rpm for 2 min. The container with the photocurable resin was immediately wrapped with aluminum foil and stored in a dark cabinet to prevent undesired light-induced reactions. The ceramic resin remained suitable for use even the following day, when leftover resin from the printing process was reused.

2.4. Printing process

The printer utilized to fabricate the green bodies was a commercial SLA SL1S SPEED (Prusa Research) with a bottom-up configuration operating at a wavelength of 405 nm and light intensity of 2.2 mW/cm^2. This machine featured a 5.96" monochrome LCD with a resolution 2560 × 1620 p.

Table 2
Composition of the ceramic resins in terms of volume percentage and their corresponding printing parameters.

	48 vol% alumina	56 vol% alumina
Monomer (HDDA and PEGDA250 in 1:1 wt ratio)	28.56	23.56
Camphor	19.90	16.40
Dispersant (BYK-111)	3.28	3.84
Photoinitiator (Omnirad 819)	0.26	0.21
Printing parameters		
Layer thickness	50 µm	50 µm
Layer exposure time	3 s	4 s
First layer exposure	20 s	20 s
Lift speed	Faster	Slower

The customizable printing parameters are as follows and have been summarized in Table 2:

- Layer thickness, set to 50 µm.
- "Layer exposure time", which is the time for which a generic layer would be exposed to the UV light. In our case, it was set between 3 – 4 s: the lowest value for the 48 vol% resin and the highest one for the 56 vol% resin.
- "First layer exposure time", which is the time for which the first printed layer would be exposed to the light. It was usually set to higher values (20 s) with respect to the previous parameter, to ensure better adhesion between the green body and the building platform.
- The "setting" of the printer (also known as lift speed or z-axis speed), which determines how fast the build head moves when it rises to detach the printer layer from the vat bottom and then descends again to prepare for the new layer. For resins with high ceramic loadings (56 vol%), it was necessary to change the setting from "Faster" to "Slower" and eventually "High viscosity" to achieve a successful and high-quality print, but at the cost of longer printing time. Resins with sufficiently low viscosity (i.e., less than 50 vol% alumina) could be printed setting the machine to "Faster", significantly shortening the duration of the printing operation.

The optimal value of these parameters was determined and used for each resin composition and for each printed geometry. It should be noted that the build head was covered in a thin layer of PTFE-based grease prior to printing to make detachment of the printed objects easier.

Two resin formulations with different solid loadings were chosen to fabricate the final samples: 48 vol% and 56 vol% alumina, both based on a resin composed of HDDA and PEGDA250 with a 1:1 monomer ratio, and the detailed compositions are reported in Table 2. There were no issues related to the sedimentation as the prepared ceramic resins were typically used shortly after preparation, either on the same day or, at most, the following day.

The samples were printed in the shape of hollow cylinders (nominal external diameter 7 mm, height 7 mm and wall thickness 1.2 mm), and a thin bowl-shaped geometry (nominal external diameter 12.5 mm, height 2.5 mm and wall thickness 0.42 mm), as shown in Fig. 1.

2.5. Post-processing

Once the printing was completed, the samples were carefully detached from the build head with a razor blade and cleaned to remove the residual unpolymerized resin from the surface. After testing with several solvents (ethanol, isopropanol, acetone, propylene carbonate and 2-phenoxyethanol), it was decided to rinse the samples with water (1 min manual stirring) and gently clean with a soft brush and an air jet. Immediately after cleaning, they were inserted in a UV-chamber

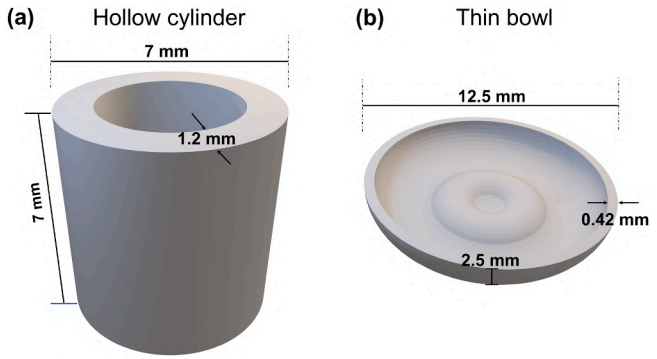

Fig. 1. CAD design of the samples to be printed.

(Robotfactory) for a post-curing operation ranging from 2 to 4 min.

The green (cylindrical) bodies underwent thermal debinding and pre-sintering in a tubular furnace (Zetasinter, Zetamix by Nanoe) in argon atmosphere. The heating rate was set to 1 °C/min (for 48 vol% alumina) and 2 °C/min (for 56 vol% alumina) until 1000 °C, then they were held at the temperature for 1 h. The samples were then conventionally sintered at 1500 °C, 1550 °C, and 1600 °C for 1 h in air at a heating rate of 10 °C/min in a muffle furnace (Nabertherm) and naturally cooled to room temperature.

The UHS experiments were carried out with a custom-made UHS set-up, as reported in our previous study [20]. Each sample was sandwiched between two graphite felt strips (SGL Carbon Co.) measuring 24 × 6 mm^2. The graphite strips were placed between two steel electrodes with a separation distance of 24 mm and connected to an AC power supply (Item 3484, TECNA).

In this work, two types of UHS experiments were performed, namely (i) *single-step* UHS: the power supply is directly ramped to the preset maximum power (240 W) and (ii) *multi-step* UHS: the applied power is increased progressively in multiple steps (40 W for 60 s, 80 W for 60 s, 120 W for 60 s, 160 W for 60 s, and 240 W for 60 – 300 s) with holding times until the desired maximum power is reached. These terms are introduced here only to distinguish the heating profiles used in this study and are not intended as general classifications of the thermal treatment process in ceramic processing.

The measurement of temperature during such rapid sintering techniques remains challenging [36]. Nevertheless, to estimate the temperature reached during the UHS process, the power required to melt around 10 – 20 mg of certain high-purity metals (Copper - Cu, Nickel - Ni, Platinum - Pt) was measured and reported in Table 3. The melting point of Ni was considered to be 1326 °C, which corresponds to the Ni-C eutectic, since SEM analysis after melting consistently revealed a reaction between Ni and C. In our experiments, 240 W can be approximated to a graphite felt temperature close to 1700 °C. The intermediate powers at 40 W, 80 W, 120 W, and 160 W can be approximated to 500 °C, 870 °C, 1150 °C, and 1401 °C, respectively, by extrapolating the temperature data reported in Table 3.

The samples processed using UHS are categorized as follows:

(i) First, the debinded cylindrical samples (Fig. 1(a)) fabricated with 56 vol% alumina were sintered in Ar atmosphere with our custom-made UHS set-up. The samples were subjected to a single-step UHS process. The average value of the power at the steady state was 240 W. The holding time was the other key parameter of the process, and was set to 60, 300, and 600 s, respectively, for different samples. The total duration of the experiments ranged from 60 s to 600 s, excluding the cooling time. The cooling time varies depending on the final temperature, but the sample could be taken out after wating for around 1 min. Green cylinders were also subjected to *single-step* and *multi-step* (the conditions are mentioned below in point (ii)) UHS experiments, but unfortunately, they could not survive such rapid heating rates.

(ii) Second, the green thin bowl-shaped samples (Fig. 1(b)) were subjected to both *single-step* and *multi-step* UHS process. These samples were debinded and sintered using the UHS in both single-step (240 W 60 s) and multi-step (40 W for 60 s, 80 W for 60 s, 120 W for 60 s, 160 W for 60 s and finally 240 W for 60 – 300 s) UHS process. The total duration of the experiments ranged from 300 to 600 s (depending on the holding time at the maximum power). This does not include the cooling time. The green samples subjected to *single-step* UHS process resulted in severe defects after the sintering.

Table 3
Melting temperatures of selected metals and corresponding power dissipation required to melt them. These temperature calibration experiments were carried out with felt size similar to the ones used for the real experiments.

Metal	Melting temperature (°C)	Power dissipated (W)
Cu	1080	109
Ni-C	1326	150
Pt	1780	250

The heating rate in the single-step UHS process can be approximated to about 1680 °C/min, whereas for the multi-step process it varies from approximately 250 – 480 °C/min. It should be noted that two samples were tested for each UHS condition.

2.6. Characterization

A rotational rheometer (Kinexus prime lab+, Netzsch) with parallel plate configuration was used to characterize the resins in a range of shear rates between 0.01 and 100 s^{-1} at 25 °C. A plate with 40 mm diameter was used and the gap between plates was set to 0.5 mm. Viscosity (η) and shear stress (τ) measurements were performed using a shear rate ramp from 0.01 to 100 s^{-1} at room temperature. The shear stress *vs.* shear rate curves detailing the effect of different solid loadings on the behavior of the suspension were fitted with the Herschel-Bulkley model [37]:

$$\tau = \tau_0 + k \bullet \dot{\gamma}^n \quad (1)$$

where τ is the measured shear stress, τ_0 is the initial yield stress, k is the consistency factor, $\dot{\gamma}$ is the true shear rate, and n is the flow index.

Thermo-gravimetric analysis (TGA) and differential scanning calorimetry (DSC) of the printed samples and of camphor was carried out using STA 449 F3 Jupiter (Netzsch, Germany) in Ar atmosphere with a heating rate of 10 °C/min.

Optical microscopy (AxioCamERc 5 s, Carl Zeiss Microscopy, US) was used to evaluate the presence of defects in the printed parts. The dimensions of the samples were measured by means of a digital caliper with a sensitivity of 0.01 mm before debinding and after sintering, to evaluate the linear shrinkage.

The relative density (ρ) of the debinded and sintered parts was measured with Archimedes' method following ASTM C 830 as a reference with some changes, using the formula:

$$\rho = \frac{\rho_b}{\rho_{Al2O3}} \frac{m_{dry}}{m_{wet} - m_b} \quad (2)$$

where ρ_b is the density of the buoyant medium (water at room temperature) that was approximated to 1 g/cm^3, ρ_{Al2O3} *is* the density of alumina, which was considered equal to 3.99 g/cm^3 [38], m_{dry} is the mass of the dry sample, m_{wet} is the mass of the sample measured after soaking it in water for 10 min under vacuum, and m_b the mass measured while the sample was immersed in water. The vacuum was obtained with a venturi pump that managed to reach the set level of about 0.064 kPa.

The phase composition of the alumina powders, of the samples sintered conventionally and of the samples consolidated through UHS was examined by X-ray diffraction (XRD) using a D8 ADVANCE diffractometer (Bruker) in the 2θ-range of 10–80° ($\Delta(2\theta) = 0.02°$ with a scan time of 1 s/step) using 15 Cu K_α radiation (λ = 1.5418 Å). The X-ray source operated at 40 kV and 40 mA. Raman spectra was recorded with a Raman Witec alpha 300 R, using a 532 nm laser with a 50 × objective to check for the presence of the residual carbon.

A mercury intrusion porosimeter (Carlo Erba) was used to determine the pore size distribution of the printed sample and sample exhibited to 220 °C for 4 h. The cylindrical samples were used for the tests.

The morphology and fracture surface of the sintered parts were analyzed through scanning electron microscopy (SEM, Solaris, Tescan) after sputtering with 70 nm of chromium to obtain the microstructure and check for the presence of defects.

The Vickers microhardness of the cylindrical sintered samples was

measured in five different regions on the polished cross-section (cutting the sample into halves along the X–Y plane) using a FM-310 microhardness tester with a load of 2 kgf for 15 s.

3. Results

3.1. Selection of monomers, and optimization of the amount of camphor

The resin must display high optical transmittance at the wavelengths at which the printer operates to obtain an adequate curing depth. The optical properties of the suspensions are determined from those of the constituent monomers. As it can be seen from the transmittance curve in Fig. 2(a), the monomer that shows the highest transmittance at a wavelength of 405 nm is HDDA, followed by PEGDA 575 and PEGDA 250, whose curves practically overlap in this region. TEGDA shows the worst optical properties out of all the monomers considered, and was therefore excluded from the resin formulation from this point onward.

The solubility of camphor in different resin compositions was investigated to better exploit the positive effect of the diluent on the suspension viscosity. The optical appearance of the resulting mixtures is reported in Table 4. The HDDA/PEGDA250 solution shows the highest solubility of camphor, with camphor dissolving up to a ratio of 1.5, while it remains undissolved at 1.3, as shown in Fig. 2(b). The other two monomer mixtures show limited camphor solubility, as evident from the resin-to-camphor ratios of 2 for HDDA/PEGDA575 and 1.7 for HDDA/TEGDA reported in Table 4. The highest camphor solubility, combined with the lowest viscosity and easy detachment from the printing platform, therefore led to the selection of the HDDA/PEGDA250 resin mixture for further experiments. The camphor content was fixed at an intermediate ratio of 1.6 to maintain a safety margin and always ensure complete dissolution.

3.2. Rheological characterization

While HDDA exhibited the best optical properties and a sufficiently low viscosity, it was found that samples printed from HDDA-based compositions were extremely difficult to detach from the building platform of the printer. A significant force needed to be applied and this often resulted in damages to the samples, which consequently were unfit for further experiments. Moreover, HDDA is reported to generate internal stress due to its high polymerization shrinkage [39].

To solve this problem, different resin compositions were investigated. HDDA/PEGDA250 and HDDA/PEGDA575-based resins, both with 1:1 monomer weight ratio. The HDDA-based resin showed the lowest viscosity (see Fig. 3(a)), but the other two resins still had sufficiently low viscosity (but higher than pure HDDA) to be suitable for VPP.

Table 4
Summary of visual appearance of the different mixtures for each resin/camphor ratio.

	Resin/camphor weight ratio			
	2	1.7	1.5	1.3
HDDA/PEGDA250	Clear	Clear	Clear	Undissolved
HDDA/PEGDA575	Clear	Undissolved	Undissolved	-
HDDA/TEGDA	Clear	Clear	Undissolved	-

Both PEGDA250 and PEGDA575 proved effective in facilitating the detachment of the printed samples from the building platform. The resin based on the HDDA/PEGDA250 mixture exhibited slightly lower viscosity (intrinsic viscosity of PEGDA250 is low compared to PEGDA575 as reported in Table 1). Therefore, this resin composition was selected for further optimization.

The efficacy of camphor was verified by comparing the rheological behavior of resins with two different ceramic loadings, both with camphor and without camphor. The viscosity *vs*. shear rate curves in Fig. 3(b) show that the resins with camphor are characterized by much lower viscosities than those without camphor [12,13]. The diluent effect is particularly evident in the resins with 56 vol% alumina; the one without camphor does not satisfy the requirement of viscosity lower than 3 Pa s at a shear rate of 30 s^{-1} [40,41] and hence could not be printed, while the resin with camphor was printable.

Ball milling of the resin is an efefctive way to break down aggregates formed by the ceramic particles and to homogenize the suspension. The optimal ball milling time was determined by comparing the rheological curves shown in Fig. 3(c). All curves exhibit shear thinning behavior and viscosity lower than 3 Pa s at a shear rate of 30 s^{-1} [40,41], thus displaying suitable behavior for VPP. It was observed that increasing the ball milling time from 30 min to 120 min resulted in a decrease in viscosity. Further increasing the ball milling duration to 240 min increased the viscosity. This indicates that ball milling beyond 120 min does not provide any significant improvement and worsens the rheological behavior of the resin when the time approaches 240 min.

The use of a dispersant ensures that the ceramic particles in the resin remain well dispersed and prevents sedimentation. It is evident in Fig. 3(d) that a higher amount of dispersant (> 2 wt%) caused an increase in viscosity [42]. The resin with 2 wt% dispersant was that with the lowest viscosity and therefore was chosen as the optimized amount of dispersant to be used for the preparation of the final samples. The dispersant content below 2 wt% were not tested, as a recent study [34] using alumina powder with a similar particle size and the same dispersant (BYK-111) reported that suspensions containing 1 wt% dispersant exhibited extremely high viscosities, making it unsuitable for printing.

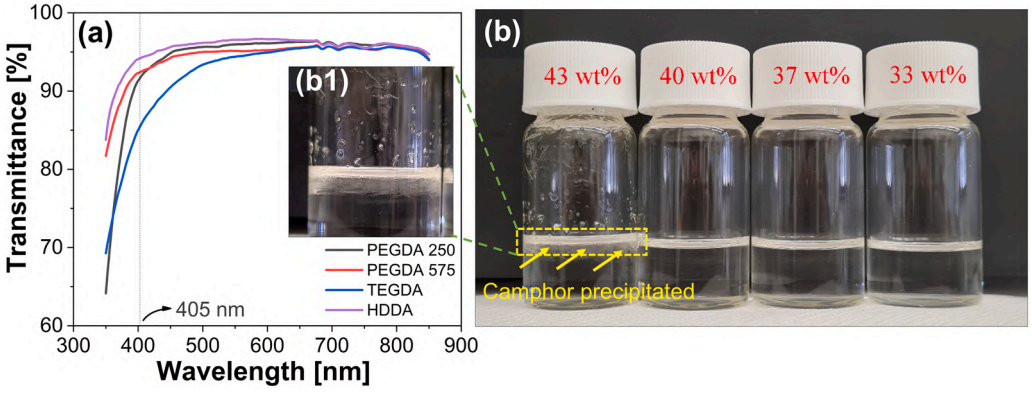

Fig. 2. (a) Transmittance curves of the monomers HDDA, TEGDA, PEGDA250, and PEGDA 575. The dotted line represents the 405 nm wavelength. (b) Photograph of the monomer mixtures prepared to evaluate the solubility of camphor in a HDDA/PEGDA250 resin with 1:1 monomer weight ratio. From left to right, the resin/camphor weight ratio is 1.3, 1.5, 1.7, 2; the camphor content with respect to the total weight of the mixture is reported on the cap of each container. The inset (b1) represents a magnified image of the phase separation between camphor and the resin.

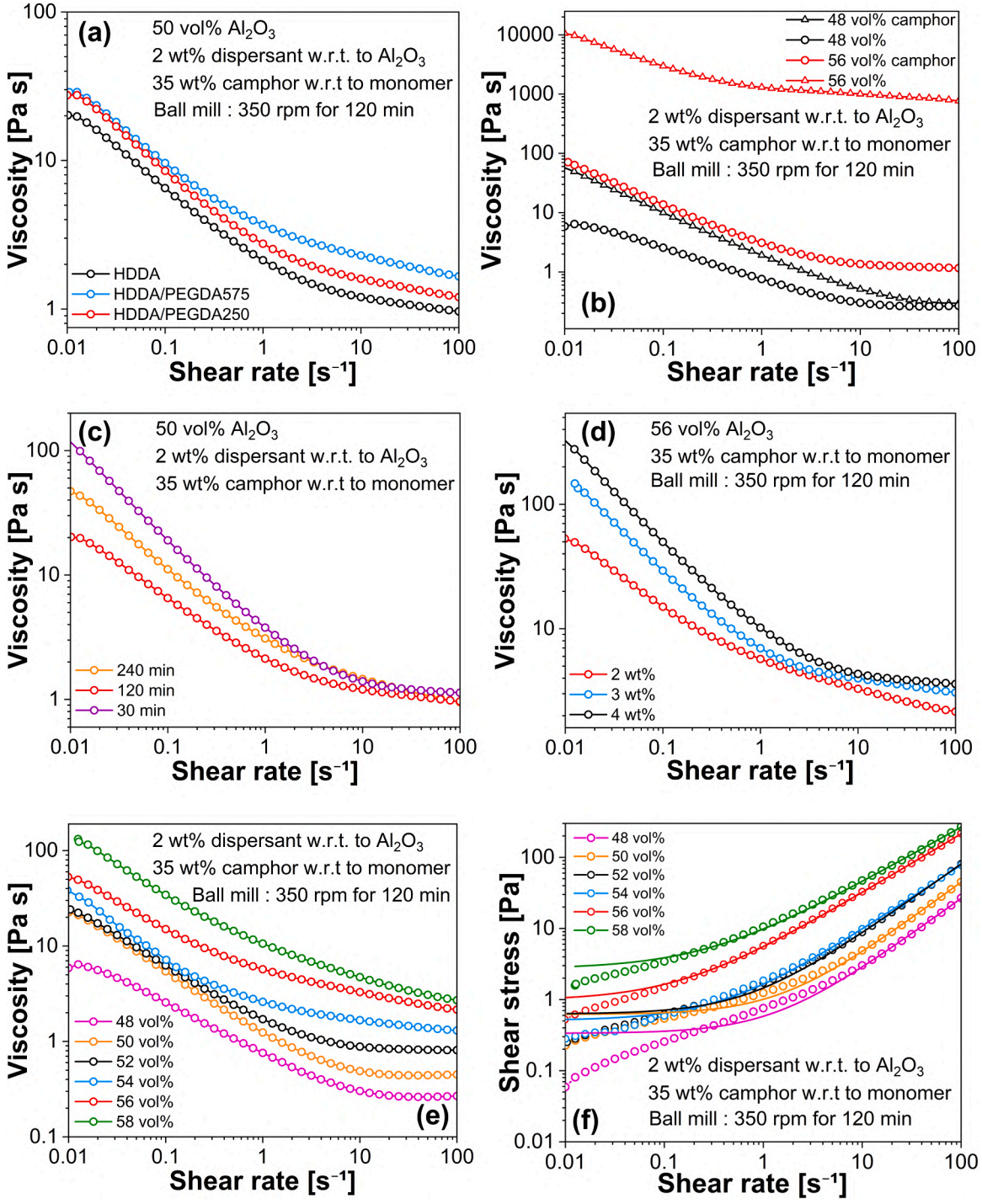

Fig. 3. Rheological analysis showing the effect of (a) monomer mixtures, (b) camphor, (c) ball milling duration, and (d) dispersant content. The effect of ceramic loading on (e) viscosity and (f) shear stress as a function of shear rate. The continuous lines in (f) represent the Herschel-Bulkley fitting.

The effect of solid loading on the rheological behavior was studied in the range of 48 – 58 vol% of alumina. All resins exhibited shear-thinning behavior as shown in Fig. 3(e). This is an ideal characteristic for ceramic VPP. Increasing the solid loading causes higher viscosity at all shear rates. All resins satisfied the requirement of having a viscosity lower than 3 Pa s at a shear rate of 30 s^{-1} [40,41] except for that with 58 vol% alumina; therefore, the preferred solid loading chosen for this study was the highest possible that satisfied this requirement, that is 56 vol%.

Fig. 3(f) reports the shear stress-shear rate curves fitted with the Herschel-Bulkley model. The values of the fitting parameters are reported in Table 5. The yield stress, τ_0 (with the exception of 54 vol%)

Table 5
Fitting parameters of the Herschel-Bulkley model for resins with different ceramic loadings.

Solid loading	τ_0 [Pa]	k [Pa s^n]	n	R^2
48 vol%	0.33 ± 0.04	0.24 ± 0.02	1.010 ± 0.010	0.99913
50 vol%	0.62 ± 0.05	0.39 ± 0.13	1.020 ± 0.007	0.99953
52 vol%	0.63 ± 0.04	0.83 ± 0.01	0.990 ± 0.003	0.99989
54 vol%	0.51 ± 0.03	1.13 ± 0.01	0.910 ± 0.002	0.99919
56 vol%	0.96 ± 0.11	4.59 ± 0.05	0.830 ± 0.003	0.99991
58 vol%	2.69 ± 0.27	7.12 ± 0.15	0.780 ± 0.005	0.99968

and the consistency index k increased as the solid loading increased. In general, the value of n decreases as the solid loading of the resin increases [7]. Most suspensions showed n < 1, confirming the observation of shear thinning behavior, except for the 48 – 50 vol% resin, whose n was about 1. The R^2 of the Herschel-Bulkley model was higher than 0.999 for all resin formulations, indicating a high degree of reliability for the fitting.

Although the behaviour observed at 54 vol% appears unusual, similar non-monotonic trends have been reported in Fig. 9 of Ref. [43]. The slight decrease in yield stress at moderate solid loading could result from particles rearranging into a more effective packing arrangement [44]. Improved packing may decrease the effective interactions between particles and lower the yield stress of the suspension before the system reaches the jamming threshold at increased solid fractions. At this stage, any hypothesis remains speculative, and a comprehensive understanding of this behaviour would require more detailed rheological analyses combined with high-resolution microstructural characterization techniques.

3.3. Post-processing: cleaning the green samples

Different solvents were employed to estimate their effectiveness at removing residual resin from the printed bodies. Different organic solvents, such as ethanol, isopropanol, acetone, propylene carbonate, and 2-phenoxyethanol resulted in severe delamination immediately after the cleaning. Water was not very effective by itself, but its efficacy was improved with the use of a soft toothbrush, which mechanically removed the residual resin from the surface of the printed samples without inducing any major delamination. The soft toothbrush did not affect the surface integrity of the samples as shown in Fig. S1. Thereafter, the samples were exposed to gentle air pressure to remove any residual uncured resin.

Even when cleaning with an appropriately non-aggressive solvent (water), the samples tended to delaminate over the course of time; therefore, the effectiveness of a post-curing operation was investigated. Samples were post-cured for different durations (0 – 4 min), and then they were analyzed with an optical microscope to evaluate the presence of defects. A curing time of 2 min was insufficient because the samples still exhibited delamination. Samples cured for 4 min showed no defects. For these reasons, post-curing for 4 min was deemed necessary to reduce or eliminate defects in the printed samples.

In Fig. 4 it is possible to compare a sample that was not post-cured (Figs. 4(a – a1)) after being removed from the printer and with a sample that was subjected to post-curing for 2 – 4 min (Figs. 4(b – b1)). The former presents evident delamination and is unsuitable for further thermal treatments. Starting from a green body with severe delamination would result in a final ceramic body of low quality. Conversely, the sample that was post-cured shows no macroscopic defects and is a good starting point for the production of a dense ceramic object. Notably, the rim at the bottom originates from the printing process parameters specially used to achieve a good adhesion to the build platform.

3.4. Thermogravimetric and mercury porosimetry analyses

TGA was performed to study the thermal decomposition behavior of camphor and of the green bodies with 48 vol% and 56 vol% alumina. It is clearly evident from the inset in Fig. 5(a) that the camphor sublimes completely at 200 °C and thereafter no mass loss can be observed. The presence of camphor in the green bodies is evidenced by an early mass loss, whereas the sample where camphor was intentionally removed

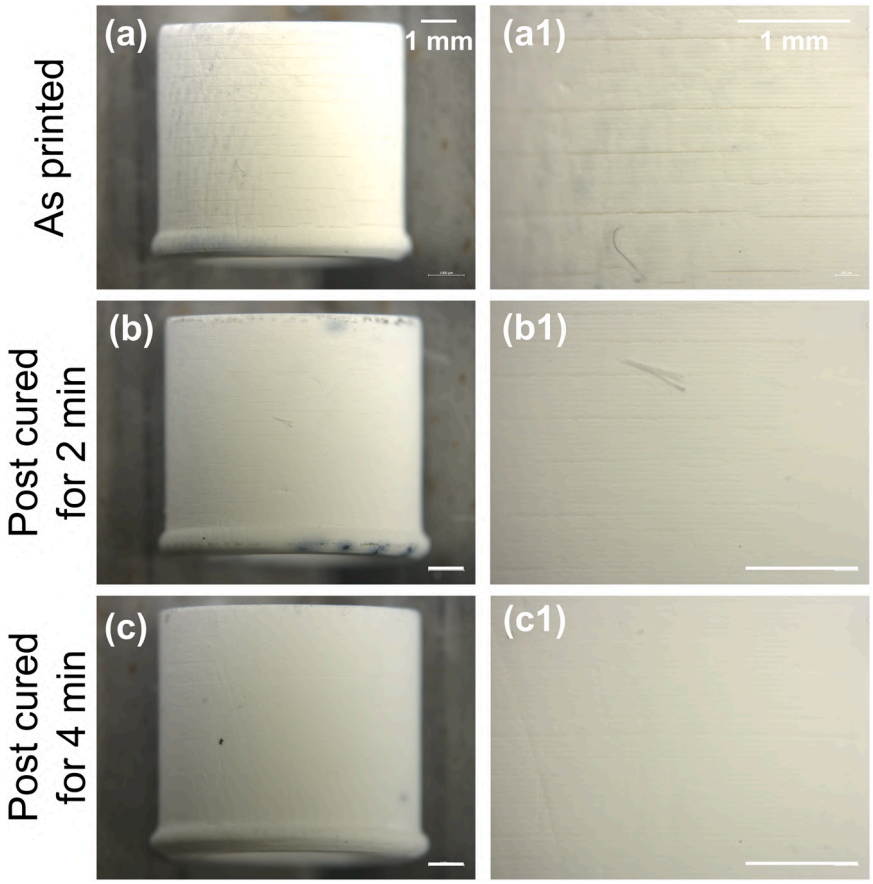

Fig. 4. Optical images of the (a) as-printed sample (no curing), (b) sample cured for 2 min, and (c) sample cured for 4 min. All samples were cleaned after printing. Images within each group [(a–c), (a1–c1)] share the same scale bar, though the scale differs between groups.

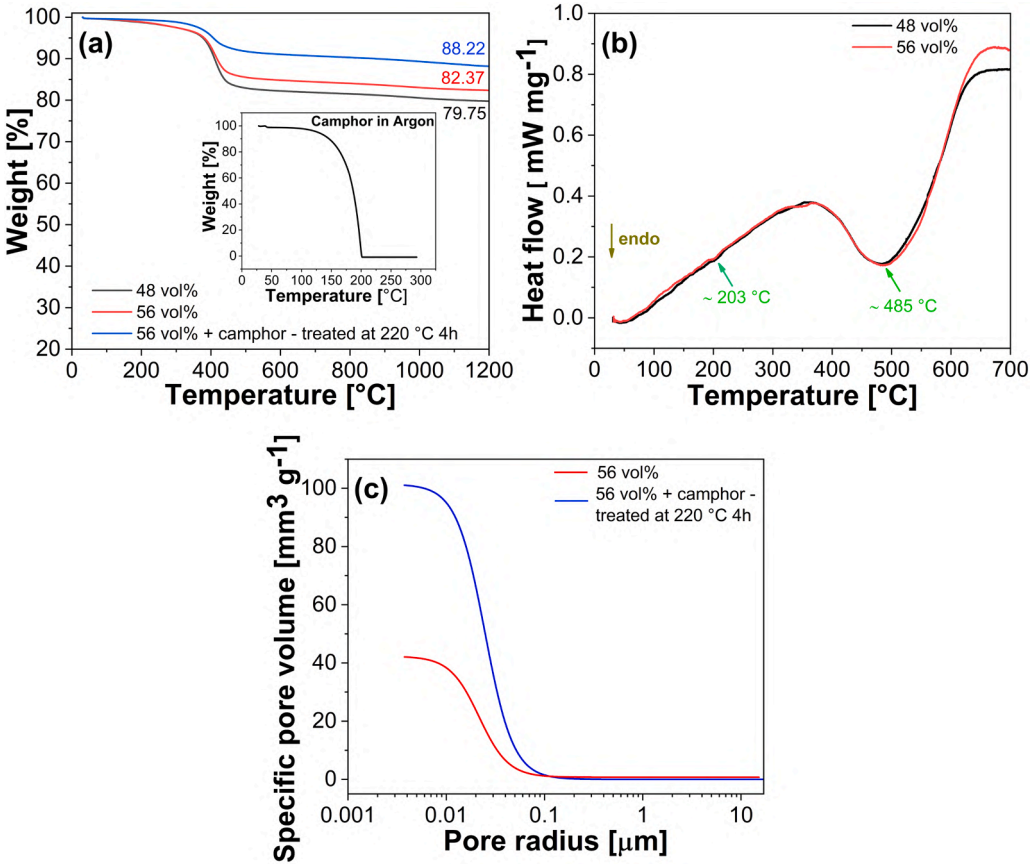

Fig. 5. (a) Thermogravimetric analysis of the printed green sample with 48 and 56 vol% ceramic loadings. For comparison, a sample with 56 vol% was treated at 220 °C to verify its stability. The inset figure shows the decomposition behavior of the camphor used in our work. (b) DSC analysis of the green sample with 48 and 56 vol % ceramic loadings. (c) Mercury porosimetry analysis of green samples fabricated with 56 vol% ceramic, and of the green sample with 56 vol% ceramic treated at 220 °C to remove the camphor.

after treatment at 220 °C exhibits mass stability up to higher temperatures (Fig. 5(a)). The most intense mass loss occurs between 350 – 500 °C, with the highest mass loss rate observed at around 420 °C for both compositions. With increasing temperature and beyond 500 °C, negligible mass loss is observed, denoting that the organic fraction was almost completely decomposed. As expected, the residual mass observed for the 56 vol% samples at the end of the process is higher than the mass observed for the 48 vol%.

The DSC curve in Fig. 5(b) reveals that the decomposition behavior is predominantly endothermic, with two main peaks. The first peak at approximately 200 °C corresponds to the volatilization of camphor, while the second peak at around 485 °C is associated with the decomposition of the resin and other organic additives. Under inert conditions the decomposition process typically shows mainly one endothermic peak (which also agrees with our measurement), whereas decomposition in air generally results in multiple strong exothermic peaks due to oxidative reactions [45].

The mercury porosimetry results are in good agreement with the TGA analysis. One can clearly notice in Fig. 5(a) that the residual ceramic content in the green body treated at 220 °C is higher than the untreated green body. This is related to the sublimation of camphor (and the resulting increase in overall ceramic content) and the corresponding increase in the open pore volume of the treated sample, which is almost 2.5 times larger than that of the untreated sample, as shown in Fig. 5(b). The pore size in the range of 0.003 – 0.03 μm can be attributed to the sublimation of camphor. Further, this pore size range is also present in the untreated samples suggesting that some camphor sublimation could have taken place even during the storage of the sample.

3.5. Debinding and sintering

One of the most critical aspects in ceramic processing is the debinding step. Samples fabricated from the resin with 56 vol% alumina had an average relative density (69.2%) higher than that of the samples prepared from the resin with 48 vol% solid loading (58.2%). Therefore, lower solid loadings result in more porous structures after the removal of the binder, as highlighted by the SEM images in the Supplementary Material (Fig. S2). It is evident that samples of both compositions underwent a significant reduction in volume during the thermal treatments, as reported in Table 7. It is also interesting to note that shrinkage was higher for the samples with 48 vol% alumina when compared to the one with 56 vol% as shown in Fig. 6(a).

One can observe that for a given composition and sintering temperature, the axial shrinkage is always higher than the radial shrinkage (see Table 7). This anisotropy is caused by the layer-by-layer approach, typical of AM processes [46]. In addition, the shrinkage also increased with the sintering temperature, which is in good agreement with the density and microstructural analysis detailed later on (Table 7, Fig. 8). It can also be observed that the anisotropy in the linear shrinkage decreases with increasing solid loading, which is a critical aspect governing the shrinkage behaviour of the samples. Minimizing the sintering shrinkage is always desirable, as most cracks and defects originate during this stage, which further highlights the advantage of employing higher ceramic loadings.

Table 6 summarizes the UHS experiments carried out in this work. A single-step thermal debinding and sintering process was carried out on the cylinders; however, the samples were destroyed and fractured into pieces due to the stress generated by the large amount of decomposed

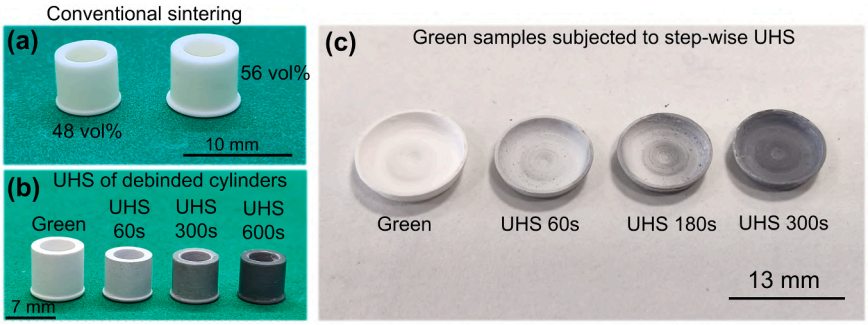

Fig. 6. Optical images of (a) conventionally sintered samples with different ceramic loadings, (b) debinded cylinders subjected to different holding times during UHS, and (c) thin bowl subjected to UHS with step-wise power for 60 – 300 s. It is to be noted that 56 vol% ceramic loading was used to fabricate samples shown in (b) and (c).

Table 6
Summary of the UHS debinding and sintering experiments carried out in this work with 56 vol% of ceramic loading in the photocurable resin.

Sample	Condition	UHS *single-step*	UHS *multi-step*
Thick cylinder[@]	Green[$]	Defects	Defects
	Debinded[#]	**No defects**	-
Thin bowl[&]	Green[$]	Defects	**No defects**
	Debinded	No experiments carried out	

@: sample with 1.2 mm thick wall
&: sample with 0.42 mm thick wall
#: samples were debinded in a conventional furnace prior to UHS
$: printed samples directly subjected to UHS

gases. Even when the power was increased in a step-wise manner, the samples retained their overall geometry but still exhibited numerous defects, particularly delamination (Fig. S3). Therefore, the cylinders were debinded first and then sintered using the UHS as shown in Fig. 6 (b).

A shrinkage trend similar to conventional sintered samples was observed for the UHS specimens: shrinkage always increases with holding time (see Table 7). The shrinkage of the UHS samples is comparable to that of materials sintered conventionally. For instance, the shrinkage of the sample subjected to UHS for 600 s is equal to 22.4% in the axial direction and 16.4% in the radial direction, very close to the 22.0% in the axial direction and 16.8% in the radial direction of the samples sintered conventionally at 1600 °C. It can also be observed that the color of the sintered ceramic parts becomes increasingly darker as the UHS holding time increases.

Table 7
Shrinkage, density and hardness value for the sintered cylinders. These cylinders were first debinded and then sintered using UHS.

Sample description	Radial shrinkage	Axial shrinkage	Relative density	Hardness (HV)
CS 48 vol% 1500 °C	16.3 ± 0.07	23.6 ± 0.07	92.7 ± 0.17	1649 ± 72
CS 48 vol% 1550 °C	16.6 ± 0.05	25.0 ± 0.06	95.5 ± 0.16	1895 ± 59
CS 48 vol% 1600 °C	16.7 ± 0.09	25.4 ± 0.04	96.8 ± 0.27	2016 ± 117
CS 56 vol% 1500 °C	14.1 ± 0.05	18.8 ± 0.07	94.8 ± 0.19	1719 ± 49
CS 56 vol% 1550 °C	14.4 ± 0.06	19.1 ± 0.09	96.7 ± 0.17	1975 ± 71
CS 56 vol% 1600 °C	16.8 ± 0.09	22.0 ± 0.04	96.4 ± 0.28	2003 ± 135
UHS 56 vol% 60 s	13.8 ± 0.06	18.1 ± 0.07	85.9 ± 0.31	1519 ± 82
UHS 56 vol% 300 s	15.9 ± 0.07	20.5 ± 0.05	95.9 ± 0.18	2011 ± 78
UHS 56 vol% 600 s	16.4 ± 0.04	22.4 ± 0.06	97.2 ± 0.12	2126 ± 97

The relative density of the conventionally sintered and UHS samples is reported in Table 7. The samples subjected to conventional sintering show densities greater than 95%, except for the 48 vol% samples sintered at 1500 °C, whose average relative density is 92.8%. It was observed that a slightly higher relative density could be achieved by increasing the sintering temperature or by starting from a resin with higher solid loading. The relative density of the samples sintered at 1600 °C was almost the same (average of 96.8% for the 48 vol% samples and 96.4% for the 56 vol% samples), suggesting that this temperature is sufficient to remove most of the open porosity.

The sample subjected to UHS for 60 s resulted in a low relative density (84.9%), confirming that this holding time is inadequate to densify the debinded sample. Samples held for 300 s and 600 s achieved good relative densities (96.9% and 98.0% respectively), slightly higher than those obtained for the samples sintered through the conventional method. Furthermore, preliminary hardness measurements, reported in Table 7, indicate that hardness increases with density, with UHS samples exhibiting higher values than conventionally sintered samples. The hardness values reported in the present study are in good agreement with previously published data [20].

In another approach, inspired by a previous work where thin spacers were produced for cold sintering [47], UHS experiments were performed on these thin structures using both a multi-step approach (i.e., increasing the current in steps). These structures were printed using the resin with the highest ceramic loading. Similar results to those obtained for the cylinders were observed with the single-step approach, when a large number of defects was generated, as shown in Fig. S4. However, with the multi-step approach, the thin spacers could be both debinded and sintered without defects, as shown in Fig. 6(c). The sintered samples reached a densification of up to ~92 – 97% (180 – 300 s, Fig. 6(c)), depending on the applied current and hold time. This was, however, only a preliminary study aimed at evaluating the limitations of the UHS approach for debinding and sintering.

3.6. XRD and Raman spectroscopy analysis

The XRD patterns of the alumina powder, the samples sintered conventionally at 1500 °C and 1550 °C, and the samples subjected to UHS for 60 s and 300 s are shown in Fig. 7(a). All sintered samples consist of phase-pure alumina (JCPDS: 00–005–0712) and no evidence of any additional phase can be observed, which is in good agreement with the Raman spectroscopy analysis in Fig. 7(b) [48].

Further Raman spectroscopy analysis was carried out on the sintered cylinder and thin spacers to check for the presence of residual carbon (Fig. 7(b)). No residual carbon contamination was observed in the Raman spectra for the cylinder (which was already debinded prior to UHS), as shown by the missing or weak D and G peaks. However, minor carbon contaminations could be detected for the thin samples, that were

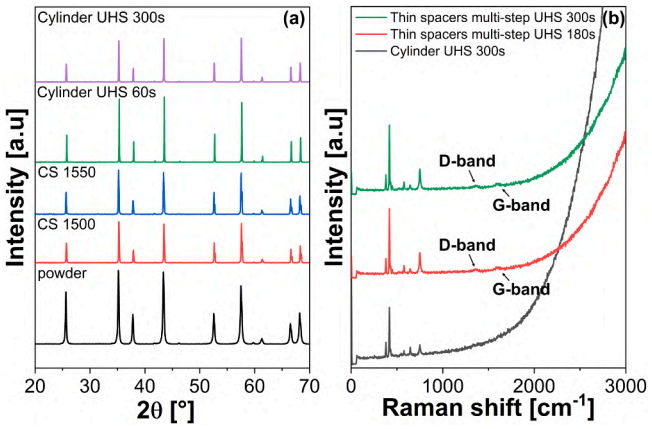

Fig. 7. (a) X-ray diffraction (XRD) pattern for the starting powder and the cylindrical samples consolidated using UHS and conventional sintering. (b) Raman spectroscopy analysis of the cylinder and thin bowl processed by UHS. These analyses were carried out on samples fabricated with 56 vol% ceramic powder in the resin.

debinded and sintered using UHS.

3.7. Microstructure

The microstructure of the sintered samples from resins with 48 vol% alumina is shown in Figs. 8(a-c, a1-c1) and that of samples with 56 vol% alumina is reported in Figs. 8(d-f, d1-f1). At 1500 °C, the microstructure is quite fine, however, some isolated porosity can still be observed at the junction of the grain boundaries. With an increase in temperature, the porosity decreases and grain growth occurs.

The microstructures of samples with different solid loadings treated at the same temperature were also compared. For sintering temperatures of 1500 °C and 1550 °C, the samples with 48 vol% alumina are more porous than the samples with 56 vol% alumina (Fig. 8(a1-b1, d1-e1)). There is instead no noticeable difference in porosity for samples of different compositions sintered at 1600 °C, consistent with the density measurement in Table 7.

Micrographs of the fracture surfaces of the cylindrical UHS samples were acquired by SEM, as shown in Figs. 8(g-h, g1-h1), to analyze the effect of different holding times on the microstructure. Longer holding times leads to a larger average grain size. The sample subjected to UHS for 60 s has an extremely fine microstructure, with grain size very close to the initial particle size of the alumina powder (Fig. 8(g1)), but a considerable amount of residual pores. With increasing power (which means increasing temperature), the porosity disappears and the samples exhibit coarser microstructure. For instance, the sample held for 300 s (Fig. 8(h1)), has a grain size and level of porosity comparable or even smaller than that of the samples with the same composition that underwent conventional sintering at 1500 °C (Fig. 8(e1)). The sample subjected to UHS for 600 s (Fig. 8(i1)) instead has a finer microstructure when compared to the samples that were sintered conventionally at 1600 °C (Fig. 8(f1)). One can also notice the change in fracture mechanism from intergranular to transgranular by increasing the sintering temperature (or grain size).

In general, the external surface of the samples subjected to UHS shows no delamination (Figs. 8(j-k, j1-k1)). The stair-case effect is evident, like in all objects produced through VPP due to the light scattering induced by the ceramic particles. The sample whose holding time was 60 s reveals some inhomogeneities, as can be seen in Fig. 8(j1), where pores are concentrated at the junction between different layers. This is not the case for the samples with holding times of 300 s and 600 s, which confirms that a correct choice of process parameters is fundamental in order to achieve good inter-layer bonding.

The fracture surface of the thin samples is shown in Fig. 8(l-m). The sample sintered for 300 s exhibits a dense microstructure, corroborating the density results. In contrast, the sample processed for 180 s is characterized by a finer microstructure with open pores.

Irrespective of the sintering method used, the SEM micrographs of some fracture surfaces reveal that delamination is present only on the external surface of the body, while the core shows good interlayer bonding (Fig. S5).

4. Discussion

The rheological properties of the resin play an important role in dictating the printing behavior, which, in turn, depends on several factors, such as the chosen monomer, ceramic loading, amount of diluent, dispersant content, and ball milling time. Monomers with better optical properties such as HDDA and PEGDA250 (Fig. 2(a)) are always desired, as they ensure sufficient UV light penetration, leading to better curing properties. However, it should be noted that the addition of the ceramic powders to the resin increase the refractive index mismatch between the resin (Table 1) and ceramic powder (R.I of alumina ~ 1.76), thereby scattering the light and decreasing the curing depth. Conversely, the addition of camphor with a refractive index similar to the resin is not expected to cause scattering of the incident radiation.

Using only HDDA as a monomer causes issues during detachment of the print head. To overcome this, a mixture of HDDA and PEGDA250 was used, which solves the problem and also exhibits lower viscosity compared to the other counterparts (Fig. 3(a)).

The curing properties can be negatively affected if the diluent (camphor) is not completely soluble. Therefore, to ensure reliability, a monomer-to-camphor ratio of 1.6 was employed, based on the optical appearance of the camphor and monomer mixtures (Fig. 2(b)). Literature also reports that camphor content up to 40 wt% in calcium phosphate (CaP) based photosensitive resin has no significant effect on the photopolymerization behavior [12].

Interestingly, the addition of camphor does not cause a pronounced decrease in viscosity at lower ceramic loading (e.g., 48 vol%). However, at higher ceramic loading (56 vol%), the reduction in viscosity becomes significant as the effective free volume for the resin molecules to move increases (Fig. 3(b)). This is in good agreement with a previous study [49]. Moreover, camphor reduces overall viscosity and flow resistance by forming a lubricating layer when flow shear force is applied [50].

Without camphor, resins at such high loadings exhibit excessively high viscosity, which leads to printing failures. Notably, the printer used in this study was a simple printer used with polymers, originally designed for low-viscosity suspensions with low UV intensity. Achieving successful printing with a ceramic resin containing 56 vol% solids is already remarkable.

The stability of the suspension is dictated by the amount of dispersant, which prevents particle sedimentation. An optimized dispersant content of 2 wt% relative to the ceramic powder was found to be optimal. Further increasing the dispersant amount leads to an excess of dispersant, causing the dispersant molecules to interact among themselves rather than with the ceramic particles, leading to an increase in the viscosity (Fig. 3(d)).

In addition, ball milling time plays a crucial role in breaking down agglomerates and ensuring homogeneous particle dispersion. A duration of 120 min results in the lowest viscosity, while further increasing to 240 min increases the viscosity (Fig. 3(c)). This suggests that excessive milling not only promotes particle size reduction due to the impact of the milling media [51], but also compromises the chemical integrity and effectiveness of the organic additives through mechanical degradation [52]. The maximum ceramic loading that could be printed with this printer was determined to be 56 vol%. All the prepared resins (except 58 vol%) satisfy the viscosity requirements of < 3 Pa s at 30 s^{-1}, ensuring the printability of the ceramic resins (Fig. 3(e)).

Once the printing process is completed, careful post-processing is required. The choice of the cleaning solvent is critical: organic solvents

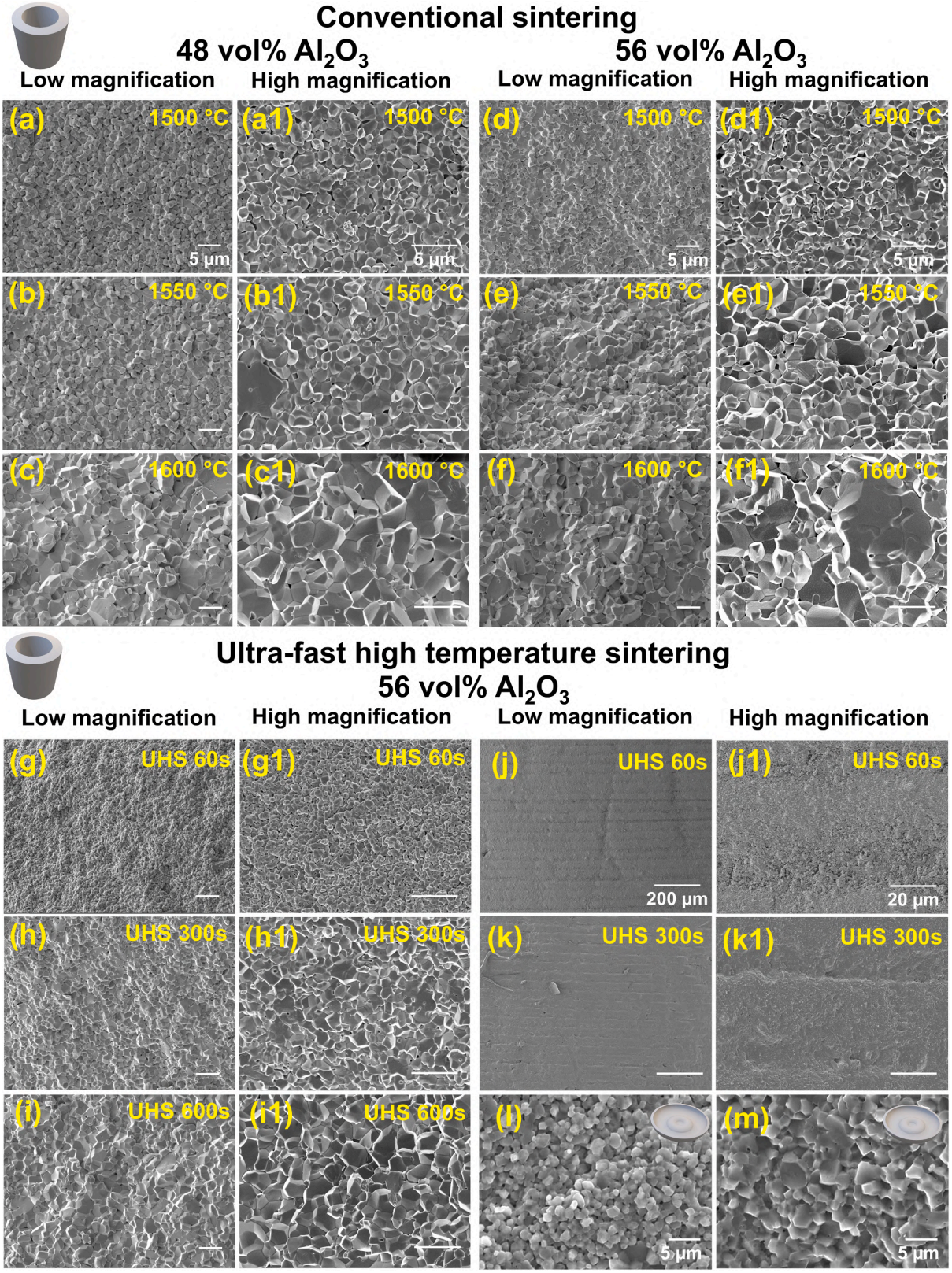

Fig. 8. SEM micrographs of the **cylindrical samples** sintered at different temperatures. (a–a1) 48 vol% at 1500 °C, (b–b1) 48 vol% at 1550 °C, (c–c1) 48 vol% at 1600 °C; (d–d1) 56 vol% at 1500 °C, (e–e1) 56 vol% at 1550 °C, (f–f1) 56 vol% at 1600 °C. Microstructures of the cylinders sintered using UHS at 240 W for (g-g1) 60 s, (h-h1) 300 s, and (i-i1) 600 s. The external surface of the samples is shown in (j-j1) and (k-k1). The fracture surface of the **thin bowl** structures processed using multi-step UHS for (l) 180 s, and (m) 300 s is also shown. Images within each group [(a–i), (a1–i1), (j–k), (j1–k1)] share the same scale bar, though the scale differs between groups.

such as ethanol, isopropanol, acetone, propylene carbonate and 2-phenoxyethanol were found to be too aggressive and led to severe delamination of the samples. These delaminations can be attributed to solvent-induced swelling of the acrylate photopolymer network. Low molecular weight and polar solvents can diffuse into the cross-linked polymer matrix and disrupt intermolecular interactions, causing volumetric expansion and internal stresses that promote cracking and interlayer delamination [53]. This phenomenon is further accelerated by the presence of camphor, which readily dissolves in these solvents (as confirmed by dissolving camphor in these solvents), enabling easier penetration of the solvents into the polymer matrix. Therefore, water was employed as the cleaning solvent, and the samples were gently cleaned with a soft brush and an air jet.

In general, higher ceramic loading results in higher green density and hence improves sintering behavior. However, increasing the ceramic loading also increases viscosity (Fig. 3(e)) (yield stress and flow index as well) and intensifies light scattering [6]. This can lead to poor interlayer bonding and consequent delamination (as the UV light intensity is fixed in the used polymeric printer). Literature reports that significant internal stresses are generated within layers during UV curing [54] and the curing efficiency is limited to 70% for a 50 vol% alumina–HDDA suspension [55]. Hence, to improve and increase the uniformity of curing conversion, a post-curing step for 4 min was also necessary to further strengthen the inter-layer adhesion and avoid delamination (Fig. 4 (c-c1)).

Thermogravimetric analysis (TGA) and mercury porosimetry further revealed the effect of camphor during debinding. Sublimation of camphor below 200 °C creates an open pore network with a volume at least 2.5 times greater than that of green samples still containing camphor (Fig. 5(b)). The presence of this open porosity facilitates smoother binder removal [17], allowing the use of relatively fast heating rates (2 °C/min) during debinding: this is already considered high for ceramic systems fabricated using VPP.

In a recent study, Huang *et al.* reported that incorporation of camphor helps to form a network of interconnected, transient pores that enable the release of decomposition gases without causing cracks [56]. Camphor also possesses a high vapor pressure at room temperature [57], it can also partially sublime during storage, as confirmed by the similarity in pore sizes between as-printed green bodies and samples intentionally treated at 220 °C to remove camphor.

The importance of the debinding step was verified by attempting to directly consolidate a green cylindrical sample through *single-step* and *multi-step* UHS. In both the cases, the samples exhibited defects, proving that despite the sublimation of camphor, the removal of the organic fraction is necessary to prevent defect formation. In the single-step UHS process where the heating rate reached ~1680 °C/min, complete shattering of the cylinder into pieces was observed (Fig. S3(a)). On the other hand, on using a multi-step profile (~250 – 480 °C/min) the samples retained their shape but exhibited visible delamination (Fig. S3(b)).

The thin bowls however survived the multi-step approach (~250 – 480 °C/min), but presented numerous defects with the single-step UHS (~1680 °C/min) as shown in Fig. S4. Either complete removal of the binder before UHS (Fig. 6(b)) or gradual decomposition during stepped heating can mitigate these stresses (Fig. 6(c)). But one has to consider the thickness limitation while processing the samples with such high heating rates [18]. Even the step-wise UHS approach failed to produce defect-free cylinders. Although it is not possible to conclusively determine a threshold wall thickness for processing by UHS, the present results indicate that samples with wall thicknesses below 420 μm can be successfully processed using a *multi-step* UHS approach, whereas samples with wall thicknesses of 1.2 mm cannot be processed even with *multi-step* approach.

When the temperature increases, the binder volatilizes and it is eventually pyrolyzed, generating gases that must be expelled from the structure. In the case of thick walls, the gases have to travel a longer path to escape and hence generate more stress [18]. This stress effect is amplified in UHS due to the extremely short times and rapid heating rates.

However, applying a stepwise current profile enabled the production of defect-free thin samples (~420 μm in green stage), supporting the hypothesis that stresses from binder decomposition are the main cause of failure. This is in good agreement with previous studies, where samples printed with a 410 μm nozzle were successfully debinded and sintered using UHS [17,18]. However, increasing the nozzle size to 580 μm and 840 μm resulted in defects, with the severity increasing with nozzle diameter [18]. It should be noted that these samples were processed using a *single-step* UHS process, thanks to the comparatively low binder content (~8 wt%) that makes the debinding process much easier compared to the present study. Further systematic experiments, increasing the wall thickness in increments of 50 – 100 μm, are required to identify the critical limits.

After UHS, the samples exhibited a pure alumina phase and typically appeared black. Raman analysis pointed out that the cylinder debinded prior to UHS does not contain carbon, confirming that the blackening is due to oxide reduction in a low-oxygen environment and longer holding times promote greater reduction of the oxide, leading to increased darkening [17,29].

On the other hand, for thin samples that were debinded and sintered together in UHS, carbon peaks are identified (Fig. 7(b)), this indicating the presence of some residual binder decomposition products. Therefore, the blackening in the thin samples can be attributed both to the reduction of the oxide and carbon contamination.

The presence of residual carbon can be associated with both the heating rates and atmosphere employed in the UHS process. The extremely high heating rate in UHS may not allow sufficient time for the binder to fully decompose and volatilize, especially considering that the binder content in the feedstock is relatively high. Moreover, the temperature was not sufficiently high to induce carbothermal reduction of alumina, which would otherwise have caused the carbon to disappear [18]. Furthermore, it is common practice to employ a two-stage debinding process [58]. In the first stage, debinding is carried out in an inert atmosphere to prevent rapid or exothermic oxidative reactions that could damage the sample. In the second stage, the samples are exposed to air to burn off any residual carbon that may remain after the initial thermal decomposition step. This indicates that when the binder decomposes in an inert atmosphere, residual carbon is often left behind as a byproduct of incomplete decomposition.

The cylindrical structures are thicker than thin-bowl shaped geometries. For the thin structures, 180 – 300 s holding time was sufficient to achieve a density of ~92 – 97% (Fig. 8(l-m)). Conversely, the cylinder (debinded before) sintered for 600 s exhibits similar density as thin bowl, which was processed for 300 s. This indicates that the thermal inertia of the sample plays an important role in the sintering process: thicker samples require more time for heat distribution when compared to thinner ones.

The microstructure of conventionally sintered samples indicates that higher ceramic loading leads to better densification. For instance, at 1500 °C, samples with 48 vol% reach ~93% density, whereas samples with 56 vol% already achieve ~95%. This indicates that samples with higher ceramic loading can reach the same level of densification at a lower sintering temperature than samples with lower ceramic loading (Table 7) [59]. As a result, the samples with 56 vol% exhibit slightly larger grain sizes due to the enhanced particle packing and faster densification kinetics (Figs. 8(a-f, a1-f1)).

A change in fracture mechanism can also be observed, from intergranular to transgranular with increasing sintering temperature or grain size for conventionally sintered samples [60]. In a fine microstructure, the larger grain boundary area makes cracks more prone to propagate along grain boundaries, especially in the presence of pores at triple points. In contrast, in a coarser microstructure with fewer grain boundaries, cracks are less likely to deflect along boundaries and instead propagate through grains. It is also worth noting that cylindrical samples

sintered by UHS exhibit a finer microstructure than their conventionally sintered counterparts, due to the rapid heating rates of the UHS process. Hence, no change in the fracture mechanism could be observed (Figs. 8 (g-i, g1-i1)). The hardness values in Table 7 are comparable to or even higher than those of the conventionally sintered samples, denoting the mechanical integrity of the sintered structures.

5. Conclusions

In this study, a photosensitive alumina resin was prepared with camphor as a diluent. A key aspect of this study is the presence of camphor in the resin, which not only drastically reduces the viscosity, particularly in the case of 56 vol% ceramic loading, but also generates open porosity before the decomposition of organic additives begins. As a result, the printed samples could withstand a heating rate of 1 – 2 °C/min, depending on the ceramic loading, resulting in a dense microstructure with ~ 97% relative density (56 vol% at 1600 °C) and Vickers hardness of ~ 2003 HV after conventional sintering.

The green cylinders (with a 1.2 mm wall thickness) exhibited defects when subjected to *single-step* or *multi-step* UHS. Therefore, the cylinders were debinded prior to the *single-step* UHS process, resulting in a finer microstructure with densities (~ 97% in 600 s) and hardness values (~ 2126 HV) comparable to those achieved by conventional sintering. Nevertheless, upon reducing the wall thickness to 420 μm in the form of a thin bowl, these samples survived the *multi-step* UHS process. Although part thickness seems to be a limiting factor for such rapid heating rates, this approach shows strong potential for thin or pre-debinded components. A notable aspect to highlight is the drastic reduction in processing time, from several hours (conventional sintering) to only a few minutes or even seconds (UHS), depending on the geometry.

Future work should focus on better understanding the threshold thickness and different complex structures (such as scaffolds) that can be debinded by UHS. Additionally, the heating rate could be further reduced with improved equipment control. The use of an air atmosphere for low-temperature debinding could also be explored to ensure complete removal of organics.

CRediT authorship contribution statement

Vincenzo M. Sglavo: Writing – review & editing, Supervision, Resources. **Paolo Colombo:** Writing – review & editing, Supervision, Project administration. **Alice Nicolini:** Writing – original draft, Investigation, Data curation. **Subhadip Bhandari:** Writing – review & editing, Writing – original draft, Visualization, Methodology, Investigation, Funding acquisition, Formal analysis, Data curation, Conceptualization. **Giorgia Franchin:** Writing – review & editing, Supervision, Resources, Conceptualization. **Mattia Biesuz:** Writing – review & editing, Supervision, Conceptualization.

Declaration of Generative AI and AI-assisted technologies in the writing process

During the revision of this work the author(s) used ChatGPT solely for language editing. After using this tool/service, the author(s) reviewed and edited the content as needed and take(s) full responsibility for the content of the published article.

Declaration of Competing Interest

The authors declare that they have no known competing financial interests or personal relationships that could have appeared to influence the work reported in this paper.

Acknowledgements

Subhadip Bhandari acknowledges the CARIPARO foundation for the PhD scholarship at the University of Padova.

Appendix A. Supporting information

Supplementary data associated with this article can be found in the online version at doi:10.1016/j.jeurceramsoc.2026.118427.

References

[1] M. Bengisu, Eng. Ceram. (2001), https://doi.org/10.1007/978-3-662-04350-9.
[2] Y. Lakhdar, C. Tuck, J. Binner, A. Terry, R. Goodridge, Additive manufacturing of advanced ceramic materials, Prog. Mater. Sci. 116 (2021) 100736, https://doi.org/10.1016/J.PMATSCI.2020.100736.
[3] A. Zocca, P. Colombo, C.M. Gomes, J. Günster, Additive manufacturing of ceramics: issues, potentialities, and opportunities, J. Am. Ceram. Soc. 98 (2015) 1983–2001, https://doi.org/10.1111/JACE.13700.
[4] ISO/ASTM 52900:2021 - Additive manufacturing — General principles — Fundamentals and vocabulary, (n.d.). ⟨https://www.iso.org/standard/74514.html⟩ (accessed September 17, 2025).
[5] Z. Chen, Z. Li, J. Li, C. Liu, C. Lao, Y. Fu, C. Liu, Y. Li, P. Wang, Y. He, 3D printing of ceramics: a review, J. Eur. Ceram. Soc. 39 (2019) 661–687, https://doi.org/10.1016/J.JEURCERAMSOC.2018.11.013.
[6] S. Zakeri, M. Vippola, E. Levänen, A comprehensive review of the photopolymerization of ceramic resins used in stereolithography, Addit. Manuf. 35 (2020) 101177, https://doi.org/10.1016/J.ADDMA.2020.101177.
[7] I.L. de Camargo, M.M. Morais, C.A. Fortulan, M.C. Branciforti, A review on the rheological behavior and formulations of ceramic suspensions for vat photopolymerization, Ceram. Int. 47 (2021) 11906–11921, https://doi.org/10.1016/J.CERAMINT.2021.01.031.
[8] A. Bove, F. Calignano, M. Galati, L. Iuliano, Photopolymerization of ceramic resins by stereolithography process: a review, Page 3591 12, Appl. Sci. 2022 12 (2022) 3591, https://doi.org/10.3390/APP12073591.
[9] H. Wu, W. Liu, R. He, Z. Wu, Q. Jiang, X. Song, Y. Chen, L. Cheng, S. Wu, Fabrication of dense zirconia-toughened alumina ceramics through a stereolithography-based additive manufacturing, Ceram. Int. 43 (2017) 968–972, https://doi.org/10.1016/J.CERAMINT.2016.10.027.
[10] J.Bin Lee, W.Y. Maeng, Y.H. Koh, H.E. Kim, Porous calcium phosphate ceramic scaffolds with tailored pore orientations and mechanical properties using lithography-based ceramic 3D printing technique, Page 1711 11, Materials 2018 11 (2018) 1711, https://doi.org/10.3390/MA11091711.
[11] R. He, W. Liu, Z. Wu, D. An, M. Huang, H. Wu, Q. Jiang, X. Ji, S. Wu, Z. Xie, Fabrication of complex-shaped zirconia ceramic parts via a DLP- stereolithography-based 3D printing method, Ceram. Int. 44 (2018) 3412–3416, https://doi.org/10.1016/J.CERAMINT.2017.11.135.
[12] Y.H. Lee, J.Bin Lee, W.Y. Maeng, Y.H. Koh, H.E. Kim, Photocurable ceramic slurry using solid camphor as novel diluent for conventional digital light processing (DLP) process, J. Eur. Ceram. Soc. 39 (2019) 4358–4365, https://doi.org/10.1016/J.JEURCERAMSOC.2019.05.069.
[13] S.Y. Yang, Y.H. Koh, H.E. Kim, Digital light processing of zirconia suspensions containing photocurable monomer/camphor vehicle for dental applications, Page 402 16, Materials 2023 16 (2023) 402, https://doi.org/10.3390/MA16010402.
[14] Y. Wu, X. Chen, G. Zhao, J. Qiu, K. Deng, J. Qiao, Y. Liu, Development of thick-walled ceramic parts via vat photopolymerization using low-viscosity non-reactive diluent as an additive, Addit. Manuf. 97 (2025) 104607, https://doi.org/10.1016/J.ADDMA.2024.104607.
[15] S. Zhou, G. Liu, A. Chen, J. Su, Y. Zhang, C. Wang, C. Yan, Y. Shi, Effect of molecular weight and chemical structure of plasticizer on suspension property, binder removal, and sintered performance for zirconia toughened alumina ceramics fabricated by vat photopolymerization, J. Eur. Ceram. Soc. 44 (2024) 116730, https://doi.org/10.1016/J.JEURCERAMSOC.2024.116730.
[16] S. Zhou, G. Liu, A. Chen, J. Su, K. Liu, C. Wang, Y. Zhang, C. Yan, Y. Shi, Defect inhibition mechanism of 3D-printed ceramics via synergetic resin composition and debinding processing regulation, J. Am. Ceram. Soc. 108 (2025) e20168, https://doi.org/10.1111/JACE.20168.
[17] S. Bhandari, C. Manière, F. Sedona, E. De Bona, V.M. Sglavo, P. Colombo, L. Fambri, M. Biesuz, G. Franchin, Ultra-rapid debinding and sintering of additively manufactured ceramics by ultrafast high-temperature sintering, J. Eur. Ceram. Soc. 44 (2024) 328–340, https://doi.org/10.1016/J.JEURCERAMSOC.2023.08.040.
[18] S. Bhandari, T. Heim, E. De Bona, V.M. Sglavo, W. Rheinheimer, M. Biesuz, G. Franchin, Rapid processing of Al2O3 ceramics by fused filament fabrication and ultrafast high-temperature debinding and sintering, J. Alloy. Compd. 1017 (2025) 178812, https://doi.org/10.1016/J.JALLCOM.2025.178812.
[19] S. Bhandari, O. Hanzel, P. Veteška, M. Janek, E. De Bona, V.M. Sglavo, M. Biesuz, G. Franchin, From rapid prototyping to rapid firing: on the feasibility of high-speed production for complex BaTiO3 components, J. Am. Ceram. Soc. 107 (2024) 6562–6573, https://doi.org/10.1111/JACE.19950.
[20] S. Bhandari, O. Hanzel, M. Kermani, V.M. Sglavo, M. Biesuz, G. Franchin, Rapid debinding and sintering of alumina ceramics fabricated by direct ink writing, J. Eur. Ceram. Soc. 45 (2025) 117144, https://doi.org/10.1016/J.JEURCERAMSOC.2024.117144.
[21] F. Lebas, L. Karacasulu, M. Biesuz, J. Lecourt, C. Bilot, S. Marinel, C. Manière, Exploration of UHS scalability by SPS approach: Multiphysics simulation, critical

dimensions, mechanisms and properties, J. Eur. Ceram. Soc. 46 (2026) 117865, https://doi.org/10.1016/J.JEURCERAMSOC.2025.117865.
[22] F. Lebas, S. Marinel, C. Manière, Ultrafast printing and sintering: breaking manufacturing speed barrier, Adv. Mater. Technol. 11 (2026) e01937, https://doi.org/10.1002/ADMT.202501937.
[23] C. Wang, W. Ping, Q. Bai, H. Cui, R. Hensleigh, R. Wang, A.H. Brozena, Z. Xu, J. Dai, Y. Pei, C. Zheng, G. Pastel, J. Gao, X. Wang, H. Wang, J.C. Zhao, B. Yang, X. Zheng, J. Luo, Y. Mo, B. Dunn, L. Hu, A general method to synthesize and sinter bulk ceramics in seconds, Science 368 (1979) (2020) 521–526, https://doi.org/10.1126/SCIENCE.AAZ7681/SUPPL_FILE/AAZ7681S2.MP4.
[24] L. Karacasulu, T. Hérisson de Beauvoir, E. De Bona, M. Cassetta, C. Vakifahmetoglu, V.M. Sglavo, M. Bortolotti, C. Manière, C. Estournès, M. Biesuz, Ultrafast high-temperature sintering of yttria-stabilized zirconia in reactive N2 atmosphere, J. Eur. Ceram. Soc. 45 (2025) 116879, https://doi.org/10.1016/J.JEURCERAMSOC.2024.116879.
[25] L. Karacasulu, C. Manière, C. Vakifahmetoglu, S. Marinel, M. Biesuz, Sintering under high heating rates, Annu. Rev. Mater. Res. 55 (2025) 203–230, https://doi.org/10.1146/ANNUREV-MATSCI-080323-042441/CITE/REFWORKS.
[26] M. Kermani, C. Hu, S. Grasso, From pit fire to ultrafast high-temperature sintering (UHS): a review on ultrarapid consolidation, Ceram. Int. 49 (2023) 4017–4029, https://doi.org/10.1016/J.CERAMINT.2022.11.091.
[27] R.F. Guo, H.R. Mao, Z.T. Zhao, P. Shen, Ultrafast high-temperature sintering of bulk oxides, Scr. Mater. 193 (2021) 103–107, https://doi.org/10.1016/J.SCRIPTAMAT.2020.10.045.
[28] A. Maria Asensio, H. Meier, A.G. Sabato, I. Babeli, L.M. Serra, S. Márquez, M. Nuñez, M. Torrell, A. Tarancón, Ultrafast sintering of 3D-printed 8YSZ for solid oxide fuel cells, J. Eur. Ceram. Soc. 45 (2025) 117674, https://doi.org/10.1016/J.JEURCERAMSOC.2025.117674.
[29] M. Mosadegh, M. Khakzad, Z. Sepasi, K. Nandigama, G. Kumar, M. Minary-Jolandan, Single-step thermal debinding for ceramics vat photopolymerization in less than 30 min, Ceram. Int. 51 (2025) 34846–34857, https://doi.org/10.1016/J.CERAMINT.2025.05.206.
[30] Z. Huang, L. Wang, R. Dou, Ultrafast high-temperature sintering of 3D-Printed yttria-stabilized Zirconia: microstructure and mechanical insights, Ceram. Int. 51 (2025) 43125–43136, https://doi.org/10.1016/J.CERAMINT.2025.07.054.
[31] F. Zuo, Q. Wang, Z.Q. Yan, M. Kermani, S. Grasso, G.L. Nie, B.B. Jiang, F.P. He, H. T. Lin, L.G. Wang, Upscaling Ultrafast High-Temperature Sintering (UHS) to consolidate large-sized and complex-shaped ceramics, Scr. Mater. 221 (2022) 114973, https://doi.org/10.1016/J.SCRIPTAMAT.2022.114973.
[32] D. Webber, A. Orth, V. Vidyapin, Y. Zhang, M. Picard, D. Liu, K.L. Sampson, T. Lacelle, C. Paquet, J. Boisvert, Printing of low-viscosity materials using tomographic additive manufacturing, Addit. Manuf. 94 (2024) 104480, https://doi.org/10.1016/J.ADDMA.2024.104480.
[33] J. Kim, Y.J. Choi, C.W. Gal, H. Park, S.Y. Yoon, H. suk Yun, Effect of dispersants on structural integrity of 3D printed ceramics, Int. J. Appl. Ceram. Technol. 19 (2022) 968–978, https://doi.org/10.1111/IJAC.13965.
[34] J.R. Verza, I.L. de Camargo, M.R. Morelli, A.P. da Luz, Development of photosensitive slurries and fabrication of alumina components using a cost-effective liquid crystal display printer, Int. J. Appl. Ceram. Technol. 22 (2025) e15123, https://doi.org/10.1111/IJAC.15123.
[35] CRC handbook of chemistry and physics, (1977). ⟨https://search.library.wisc.edu/catalog/999469374502121⟩.
[36] M. Biesuz, L. Karacasulu, C. Vakifahmetoglu, V.M. Sglavo, On the temperature measurement during ultrafast high-temperature sintering (UHS): Shall we trust metal-shielded thermocouples? J. Eur. Ceram. Soc. 44 (2024) 3479–3485, https://doi.org/10.1016/J.JEURCERAMSOC.2023.11.061.
[37] W.H. Herschel, R. Bulkley, Konsistenzmessungen von Gummi-Benzollösungen, Kolloid-Z. 39 (1926) 291–300, https://doi.org/10.1007/BF01432034/METRICS.
[38] A.M. Abyzov, Aluminum oxide and alumina ceramics (review). Part 1. Properties of Al2O3 and commercial production of dispersed Al2O3, Refract. Ind. Ceram. 60 (2019) 24–32, https://doi.org/10.1007/s11148-019-00304-2.
[39] V. Tomeckova, J.W. Halloran, Flow behavior of polymerizable ceramic suspensions as function of ceramic volume fraction and temperature, J. Eur. Ceram. Soc. 31 (2011) 2535–2542, https://doi.org/10.1016/J.JEURCERAMSOC.2011.01.019.
[40] K. Li, Z. Zhao, The effect of the surfactants on the formulation of UV-curable SLA alumina suspension, Ceram. Int. 43 (2017) 4761–4767, https://doi.org/10.1016/J.CERAMINT.2016.11.143.
[41] X. Xu, S. Zhou, J. Wu, C. Zhang, X. Liu, Inter-particle interactions of alumina powders in UV-curable suspensions for DLP stereolithography and its effect on rheology, solid loading, and self-leveling behavior, J. Eur. Ceram. Soc. 41 (2021) 2763–2774, https://doi.org/10.1016/J.JEURCERAMSOC.2020.12.004.
[42] W. Wang, J. Sun, B. Guo, X. Chen, K.P. Ananth, J. Bai, Fabrication of piezoelectric nano-ceramics via stereolithography of low viscous and non-aqueous suspensions, J. Eur. Ceram. Soc. 40 (2020) 682–688, https://doi.org/10.1016/J.JEURCERAMSOC.2019.10.033.
[43] L. del-Mazo-Barbara, M.P. Ginebra, Rheological characterisation of ceramic inks for 3D direct ink writing: A review, J. Eur. Ceram. Soc. 41 (2021) 18–33, https://doi.org/10.1016/J.JEURCERAMSOC.2021.08.031.
[44] Impact of particle packing on the rheological properties of cementitious pastes dispersed with polycarboxylate, ANNUAL TRANSACTIONS OF THE NORDIC RHEOLOGY SOCIETY 25 (2017). ⟨https://nordicrheologysociety.org/AnnualTransactions/ShowAllTransactions?selectedYear=2017⟩ (accessed March 11, 2026).
[45] P. Stastny, O. Man, D. Brouczek, M. Schwentenwein, M. Trunec, Effect of atmosphere on thermal debinding of DLP-printed ceramics, J. Eur. Ceram. Soc. 46 (2026) 117891, https://doi.org/10.1016/J.JEURCERAMSOC.2025.117891.
[46] S. Zhou, F. Zhang, J. Wu, J. Su, K. Liu, Y. Zhang, C. Wang, C. Yan, Y. Shi, Anisotropy in ceramic vat photopolymerization: formation mechanisms, influence on properties, and manipulating strategies, J. Eur. Ceram. Soc. 45 (2025) 117249, https://doi.org/10.1016/J.JEURCERAMSOC.2025.117249.
[47] S. Marín-Cortés, M. Biesuz, S. Bhandari, G. Franchin, E. Enríquez, J.F. Fernández, V.M. Sglavo, Cold sintering of complex-shaped ceramic materials, J. Eur. Ceram. Soc. 44 (2024) 116813, https://doi.org/10.1016/J.JEURCERAMSOC.2024.116813.
[48] S. Vural, Ö. Sari, Synthesis and characterization of SDS assistant α-alumina structures and investigation of the effect of the calcination time on the morphology, Colloid Polym. Sci. 297 (2019) 107–114, https://doi.org/10.1007/S00396-018-4442-4/TABLES/1.
[49] S.Y. Yang, Y.H. Koh, H.E. Kim, Digital light processing of zirconia suspensions containing photocurable monomer/camphor vehicle for dental applications, Page 402 16, Materials 2023 16 (2023) 402, https://doi.org/10.3390/MA16010402.
[50] P. Qu, G. Liang, M.I. Hussain, M. Hanif, M. Hamza, K. Huang, Y. Lou, Z. Chen, Low-temperature fabrication of high-specific strength SiC-based ceramics via photopolymerization 3D printing with controllable anisotropy, Int. J. Extrem. Manuf. 7 (2025) 055002, https://doi.org/10.1088/2631-7990/ADD2E1.
[51] F. Mohammadi, O. Mirzaee, M. Tajally, The effects of ball milling time on the rheological, optical, and microstructural properties of YAG transparent ceramics, Int. J. Appl. Ceram. Technol. 17 (2020) 1119–1127, https://doi.org/10.1111/IJAC.13381.
[52] G. Ye, Y. Jiao, P. Zhou, J. Sun, L. Zhu, F. Gong, J. Bai, G. Liu, M. Yan, R. Zhang, Preparation of silicon carbide ceramic slurry for stereolithography based additive manufacturing, Process. Appl. Ceram. 17 (2023) 47–54, https://doi.org/10.2298/PAC2301047Y.
[53] X. Wang, J.M. Aarts, N.C.K. Heng, A.B. Cameron, J.J.E. Choi, Influence of different post-washing parameters on the properties of additively-manufactured dental devices - A systematic review, J. Dent. 165 (2026) 106315, https://doi.org/10.1016/J.JDENT.2025.106315.
[54] X. Wu, C. Xu, Z. Zhang, C. Guo, Modeling and visualization of layered curing conversion profile in ceramic mask projection stereolithography process, Ceram. Int. 46 (2020) 25750–25757, https://doi.org/10.1016/J.CERAMINT.2020.07.053.
[55] K.C. Wu, J.W. Halloran, Photopolymerization monitoring of ceramic stereolithography resins by FTIR methods, J. Mater. Sci. 40 (2005) 71–76, https://doi.org/10.1007/S10853-005-5689-Y/METRICS.
[56] K. Huang, G. Franchin, P. Colombo, Volumetric additive manufacturing of SiOC by xolography, Small 20 (2024) 2402356, https://doi.org/10.1002/SMLL.202402356.
[57] D. Schimon, S. Patakyová, P. Stavárek, P. Dzik, T. Homola, F. Zažímal, P. Klusoň, Visible-light-sensitive coatings of graphitic carbon nitride with inherent porosity induced by camphor, J. Photochem. Photobiol. A Chem. 468 (2025) 116507, https://doi.org/10.1016/J.JPHOTOCHEM.2025.116507.
[58] S. Bhandari, G. Vajpayee, L.L. da Silva, M. Hinterstein, G. Franchin, P. Colombo, A review on additive manufacturing of piezoelectric ceramics: From feedstock development to properties of sintered parts, Mater. Sci. Eng. R Reports 162 (2025) 100877, https://doi.org/10.1016/J.MSER.2024.100877.
[59] J. Cheng, Y. Chen, J.W. Wu, X.R. Ji, S.H. Wu, 3D printing of BaTiO3 piezoelectric ceramics for a focused ultrasonic array, Page 4078 19, Sensors 2019 19 (2019) 4078, https://doi.org/10.3390/S19194078.
[60] K.R. Kambale, A. Mahajan, S.P. Butee, Effect of grain size on the properties of ceramics, Met. Powder Rep. 74 (2019) 130–136, https://doi.org/10.1016/J.MPRP.2019.04.060/ASSET/IMAGES/J.MPRP.2019.04.060_GR1.JPG.